# An Experimental and Theoretical Investigation of the Inversion of Pd@Pt Core@Shell Dendrimer-Encapsulated Nanoparticles

**Rachel M. Anderson,[†,‡] Liang Zhang,[†,§] James A. Loussaert,[†,‡] Anatoly I. Frenkel,[⊥,*] Graeme Henkelman,[†,§,*] and Richard M. Crooks[†,‡,*]**

[†]Department of Chemistry and Biochemistry, [‡]Texas Materials Institute, [§]Institute for Computational and Engineering Sciences, The University of Texas at Austin, 1 University Station, 105 East 24th Street Stop A5300 Austin, Texas 78712, United States and [⊥]Physics Department, Yeshiva University, 245 Lexington Avenue, New York, New York 10016, United States

**ABSTRACT** Bimetallic PdPt dendrimer-encapsulated nanoparticles (DENs) having sizes of about 2 nm were synthesized by a homogeneous route that involved (1) formation of a Pd core, (2) deposition of a Cu shell onto the Pd core in the presence of $H_2$ gas, and (3) galvanic exchange of Pt for the Cu shell. Under these conditions, a Pd@Pt core@shell DEN is anticipated, but detailed characterization by *in-situ* extended X-ray absorption fine structure (EXAFS) spectroscopy and other analytical methods indicate that the metals invert to yield a Pt-rich core with primarily Pd in the shell. The experimental findings correlate well with density functional theoretical (DFT) calculations. Theory suggests that the increased disorder associated with <~2 nm diameter nanoparticles, along with the relatively large number of edge and corner sites, drives the structural rearrangement. This type of rearrangement is not observed on larger nanoparticles or in bulk metals.

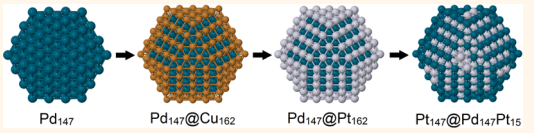


**KEYWORDS:** EXAFS · dendrimer-encapsulated nanoparticles · DFT · inversion · core@shell · PdPt

Here we report the homogeneous synthesis of core@shell $Pd_{147}@Pt_{162}$ dendrimer-encapsulated nanoparticles (DENs) and the subsequent spontaneous reconfiguration of these structures to yield an inverted $Pt_{147}@Pd_{147}Pt_{15}$ form (the subscripts represent nominal numbers of atoms in the core and shell, Scheme 1). Because these DENs undergo structural rearrangements, we will use the notation "PdPt", which does not imply a particular structure, for the as-synthesized DENs, and reserve the more specific core@shell notation "Pd@Pt" for cases where this structure has been confirmed. We have recently discovered that atomic remodeling of the sort reported here may be relatively commonplace in 1−2 nm nanoparticles,[1,2] whereas structurally similar larger nanoparticles retain stable configurations.[3−5] In addition to the inversion process, which is confirmed experimentally by *in situ* extended X-ray absorption fine structure (EXAFS) spectroscopy, there are two additional key findings arising from this study. First, the inversion process is also predicted to occur by density functional theory (DFT) calculations. Second, the synthetic approach for preparing these PdPt DENs in homogeneous solution has not previously been reported, and it opens the door to preparation of significant quantities of 1−2 nm bimetallic DENs having well-defined structures.

It has been reported that Pd@Pt nanoparticles exhibit enhanced electrocatalytic activity for the oxygen reduction reaction (ORR) compared to monometallic Pt catalysts.[4,6,7] Techniques such as high-resolution scanning transmission electron microscopy (HR-STEM),[5] Fourier-transform infrared spectroscopy (FT-IR),[8,9] and EXAFS[3,10] have been used to investigate the structure and structural stability of Pd@Pt nanoparticles within the size range of 2.0−5.0 nm. For example, Chen and co-workers prepared 4.5 nm Pd@Pt nanoparticles using a surface-limited-growth procedure. This is a three-step synthesis in which (1) Pd nanoparticles are exposed to hydrogen, thereby forming a PdH shell; (2) $Cu^{2+}$ is reduced onto the Pd surface *via*

* Address correspondence to anatoly.frenkel@yu.edu, henkelman@cm.utexas.edu, crooks@cm.utexas.edu.

Received for review August 2, 2013 and accepted September 24, 2013.

**Published online October 02, 2013**
**10.1021/nn4040348**

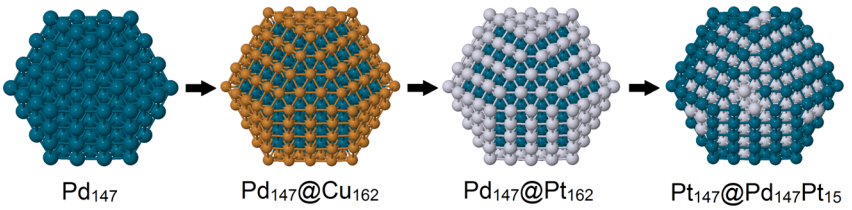


**Scheme 1. Synthetic scheme.**

cross reaction with the hydride; and (3) the $Pd_{147}@Cu_{162}$ nanoparticles are exposed to $Pt^{2+}$, which leads to galvanic exchange and formation of the final ~4.5 nm product having a Pd core and an ultrathin Pt shell.[3] We used a synthetic strategy similar to this in the present study to prepare ~2 nm $Pd_{147}Pt_{162}$ DENs.

In a study closely related to ours, Russell and coworkers reported the synthesis and structural properties of PdPt nanoparticles.[11] In this case, they started with a commercial carbon-supported Pd catalyst and used a controlled surface reaction (CSR) route to add a Pt shell. Depending on the Pt:Pd ratio, the size of the particles ranged from 2.0 to 3.4 nm. On the basis of EXAFS and electrochemical analyses, these materials were reported to have a mixed (Pd and Pt) surface composition with Pt preferentially located subsurface. This rearrangement was explained in terms of previously calculated segregation energies.[12] Other calculations on bimetallic PdPt clusters in this size range also indicate that the most stable configurations have a Pt-rich core.[13−16]

Monometallic DENs are generally prepared by a two-step process.[17,18] First, a solution containing a particular metal-ion:dendrimer ratio is prepared. This results in the metal ions partitioning into the dendrimer interior. Second, a chemical reducing agent, such as $BH_4^-$, is added to this solution. This leads to formation of a zerovalent metal nanoparticle sterically trapped within the dendrimer. The size of the DEN is strongly correlated to the original metal-ion:dendrimer ratio in the solution prepared in the first step.[19] Importantly, the host dendrimer does not interact strongly with the surface of the encapsulated nanoparticle,[20] which means DENs are catalytically active.

Our present interest is focused on synthesizing bimetallic alloy[21,22] and core@shell[23,24] DENs, and then comparing their catalytic properties to DFT calculations.[2,25,26] There are two critical conditions for such comparisons to be viable. First, the particles must be small enough to enable direct correlation to computations. Second, the structure of the particles must be very well-defined. Both of these conditions are frequently achieved with DENs. However, we have observed some unusual cases that give rise to atypical structures. A case in point is the PdAu DEN system.[1] When a $Pd^{2+}/Au^{3+}$ DEN precursor is co-reduced, stable bimetallic alloy DENs form. If $Au^{3+}$ is loaded into the dendrimer and reduced, and then $Pd^{2+}$ is subsequently added and reduced, stable Au@Pd DENs result. However, if the order of reduction is reversed, a Pd@Au DEN structure is anticipated, but the experimental finding is that the inverted Au@Pd structure results.

These prior observations for PdAu DENs are consistent with the results reported here for the PdPt system. Specifically, nominal $Pd_{147}Pt_{162}$ DENs (2.0 ± 0.2 nm) prepared by the previously discussed synthesis procedure (PdH formation, followed by galvanic exchange first for Cu and then for Pt) were examined by electron microscopy, UV−vis spectroscopy, X-ray photoelectron spectroscopy (XPS), *in situ* EXAFS, and X-ray absorption near edge structure (XANES) spectroscopy, and the results of all these analytical methods are consistent with structural inversion in which the more noble Pt partitions to the core and the shell becomes enriched in Pd. Moreover, we are now able to rationalize the structural inversion using first-principles calculations. Specifically, we present comparative thermodynamic stability calculations of different structures and segregation energies derived from swapping core and shell atoms. These calculations make it possible to propose a mechanistic route for the inversion process involving the high-energy corner and edge sites that are numerous only on very small nanoparticles. As noted earlier, larger Pd@Pt nanoparticles have stable structures, presumably due to their much smaller relative number of corner and edge atoms.

## RESULTS AND DISCUSSION

**Particle Synthesis and UV−Vis Analysis.** As described in the Methods section, G6-OH($Pd_{147}$) DENs were prepared by first complexing 147 equiv of $PdCl_4^{2-}$ to the interior of the dendrimer. The UV−vis spectrum of this precursor (Figure 1, black line) displays the expected ligand-to-metal charge transfer (LMCT) band at ~230 nm. After reduction with $NaBH_4$, the LMCT band disappears and the broad-band absorption associated with nanoparticles is observed (red line). Importantly, after the addition of $Cu^{2+}$ in the presence of $H_2$ gas (blue line), no dendrimer/$Cu^{2+}$ LMCT band is present at $\lambda_{max}$ = 300 nm,[27] indicating that $Cu^{2+}$ is not complexed to the dendrimer but rather is in its reduced form. The observed increase in the broad absorbance after adding $Cu^{2+}$ is associated with the presence of larger DENs, suggesting that Cu is present as a thin shell on the Pd DENs. After addition of $Pt^{2+}$, and the corresponding galvanic exchange of Cu for Pt, the absorbance increases again (green line). Again, no dendrimer/$Cu^{2+}$ LMCT is observed, but in this case its absence is due

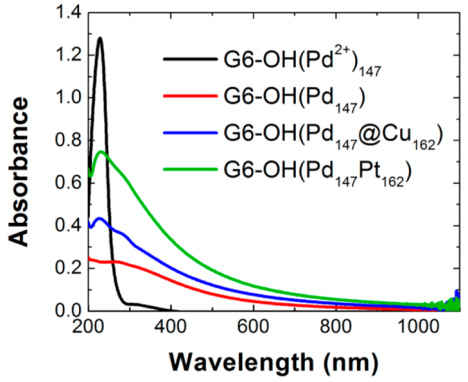


**Figure 1. UV−vis spectra of each step of the homogeneous synthesis of $Pd_{147}Pt_{162}$ DENs at a concentration of 2.0 $\mu$M in a 2.00 mm quartz cuvette, blanked with 2.0 $\mu$M G6-OH.**

to the low pH (~3) of the solution and the resulting protonation of the interior tertiary amines of the dendrimer.[27] Taken together, the UV−vis results are fully consistent with the proposed synthetic pathway illustrated in Scheme 1, though they do not provide sufficient information to infer structural details about the product.

The open circuit potential (OCP) of the synthetic process summarized by Figure 1 was also monitored and the results are provided in Figure S1. Shifts in the solution potential upon addition of each reagent are fully consistent with the conclusions of the previous paragraph.

**TEM and XPS Analysis of $Pd_{147}Pt_{162}$ Bimetallic DENs.** TEM data indicate that the initial $Pd_{147}$ DEN core has a diameter of 1.6 ± 0.2 nm (Figure 2b and Figure S2), which is consistent with previous reports and the calculated diameter of a 147-atom, closed-shell Pd cuboctahedron.[19] After addition of Pt, however, TEM analysis (Figure 2a,b) indicates an average increase in size of 0.4 nm to 2.0 ± 0.2 nm. The expected difference in diameter between Pt particles containing 147 and 309 atoms is 0.45 nm.[28] Note that the micrograph in Figure 2a was obtained after immobilizing the $Pd_{147}Pt_{162}$ DENs onto a Vulcan carbon support (see Methods for details). Figure 3a,b shows high-resolution STEM images that support the claim of monodispersity in size. Importantly, Figure 3c is an EDS line scan showing that both Pt (red) and Pd (blue) are collocated within the same particle.

Figure 4 presents high-resolution XPS scans of the Pd and Pt binding energy region for the $Pd_{147}Pt_{162}$ DENs. For Pd, two peaks are present at 335.6 eV ($3d_{5/2}$) and 341.0 eV ($3d_{3/2}$), which correspond well with those expected for fully reduced Pd DENs: 335.7 and 341.0 eV,[29] respectively. This indicates that Pd is present in its zerovalent form and does not oxidize during synthesis. For comparison, an XPS spectrum of $Pd_{147}Pt_{162}$ DENs that have been intentionally partially oxidized is provided in Figure S3. In the partially oxidized DENs, two pairs of peaks are present. One pair corresponds to zerovalent Pd and the other pair, which appears at 338.2 and 343.5 eV,[30] corresponds to $Pd^{2+}$. Note that the latter pair of peaks is absent in Figure 4a.

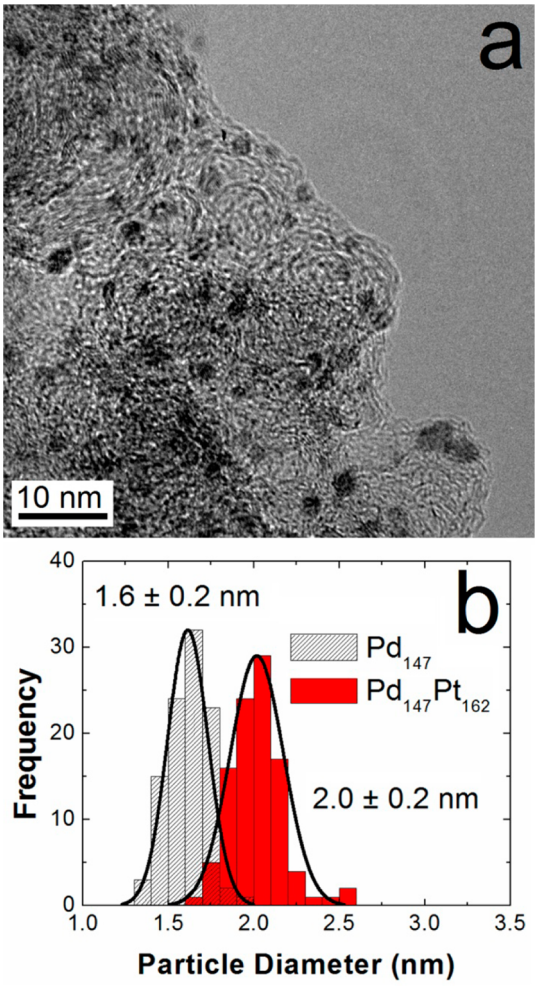


**Figure 2. (a) TEM image of the $Pd_{147}Pt_{162}$ DENs ink. (b) Size-distribution histogram of the $Pd_{147}Pt_{162}$ DENs and the $Pd_{147}$ DEN precursor showing the 0.4 nm shift in the centroid after addition of Pt.**

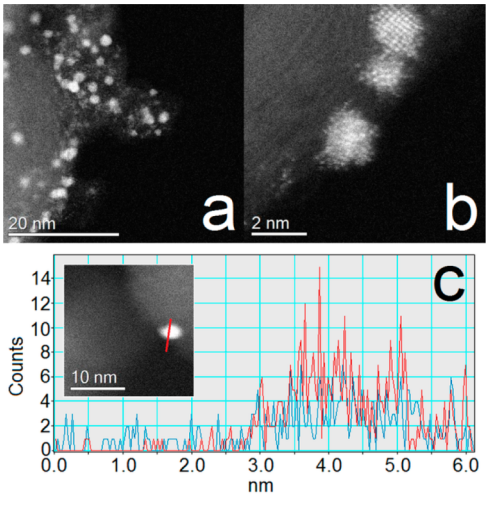


**Figure 3. (a and b) HR-STEM images of $Pd_{147}Pt_{162}$ supported on Vulcan carbon and (c) an EDS line scan of an individual particle indicating collocation of Pt (red) and Pd (blue). The inset shows the particle used for the EDS analysis.**

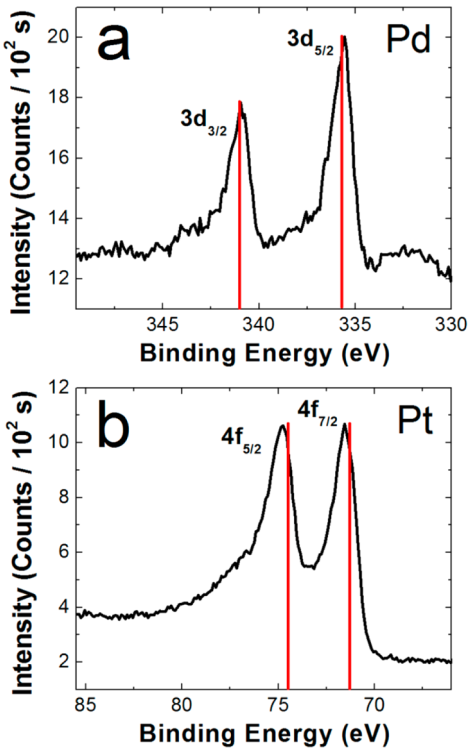


**Figure 4. High-resolution XPS spectra of $Pd_{147}Pt_{162}$ DENs in the (a) Pd and (b) Pt regions. The solid red lines correspond to the location of the binding energies for the zerovalent metals.**

Two XPS peaks are also present in the Pt 4f region for the $Pd_{147}Pt_{162}$ DENs (Figure 4b). These appear at 71.6 eV ($4f_{7/2}$) and 74.8 eV ($4f_{5/2}$), which is comparable to values previously reported for G6-OH($Pt_{55}$) DENs: 71.3 and 74.5 eV,[31] respectively. The absence of peaks corresponding to higher oxidation states of Pt indicates that complete galvanic exchange has occurred and that all of the added Pt salt has been reduced. The conclusion that both elements are located within the same nanoparticle and that they are both in their reduced form is necessary to validate the fitting model used for the EXAFS analysis presented later.

**Electrochemistry.** In Figure 5a,b, CVs of the $Pd_{147}Pt_{162}$ DENs are compared with those obtained using monometallic $Pt_{240}$ DENs. In each case, the electrode was modified with a DEN-containing ink (see Methods). A CV of the $Pd_{147}Pt_{162}$ DENs (Figure 5a) reveals H-atom adsorption and desorption at potentials between 0.3 V and the negative scan limit of 0.05 V. Upon scan reversal, the surface of the DENs is oxidized starting at ~0.8 V, and then, when the scan is reversed again, the oxide is reduced between 0.8 and 0.5 V. These types of features are characteristic of both monometallic Pd and Pt materials.[4,22,24]

The CV for $Pd_{147}Pt_{162}$ DENs can be compared to that of monometallic Pt DENs. For example, the CV obtained using monometallic $Pt_{240}$ DENs (Figure 5b) exhibits two distinct hydride peaks on both the forward and reverse scans. As we have discussed previously,

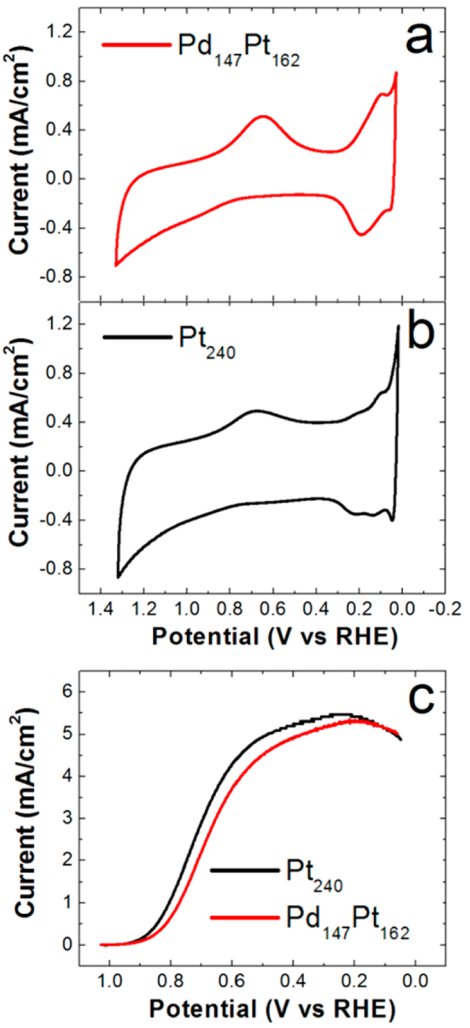


**Figure 5. CVs of (a) $Pd_{147}Pt_{162}$ and (b) $Pt_{240}$ DENs supported on Vulcan carbon. The scans started at 0.70 V and initially proceeded in the negative direction. The 20th scan is shown, the scan rate was 100 mV/s, and the electrolyte was Ar-purged. (c) RDVs showing reduction of $O_2$ using the same DEN-modified electrodes that were used for parts a and b. The electrolyte was $O_2$-saturated 0.10 M $HClO_4$. The scan started at 0.05 V and proceeded at 10 mV/s in the positive direction. The rotation rate was 1600 rpm. All current measurements are normalized to the geometric area of the electrode (0.248 $cm^2$).**

this is a consequence of faceting on larger DENs.[24] The $Pd_{147}Pt_{162}$ DENs exhibit only one adsorption/desorption feature. This has previously been observed in PdPt alloy DENs. In the latter case, increasing Pd content results in a diminution, and eventual elimination, of the second hydride feature.[22] By analogy to these early results, we conclude that the surface of the $Pd_{147}Pt_{162}$ DENs (Figure 5a) contains a significant amount of Pd.

RDV scans for the ORR at $Pd_{147}Pt_{162}$ and $Pt_{240}$ DENs are compared in Figure 5c. Here, the onset potential for the ORR at the $Pd_{147}Pt_{162}$ DEN electrocatalysts is shifted slightly negative of the $Pt_{240}$ DENs. In contrast, larger Pd@Pt core@shell materials exhibit increased activity compared to otherwise equivalent monometallic Pt nanoparticles.[4] Accordingly, the RDV data

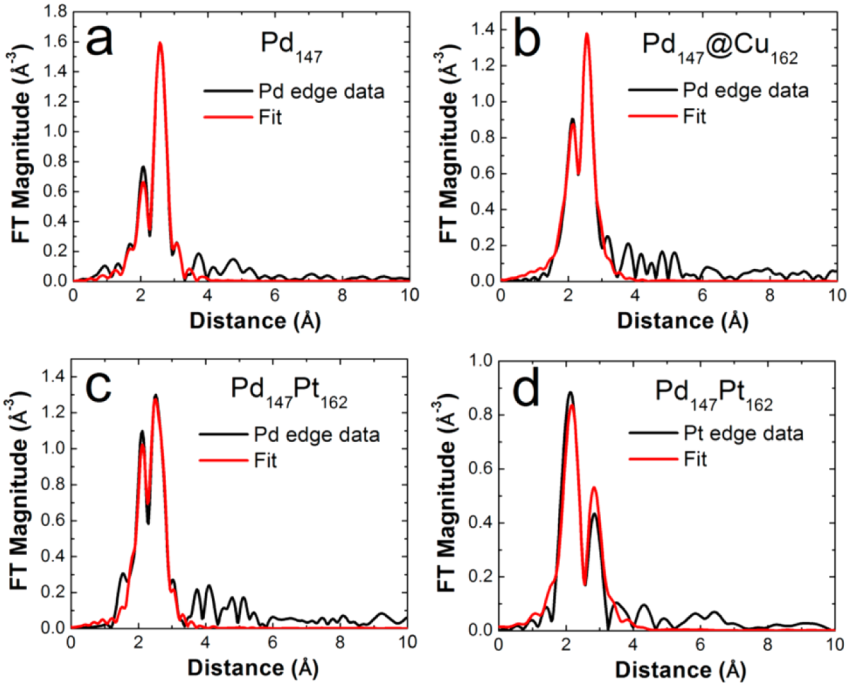


**Figure 6. EXAFS data and R-space fits (*k*-weight of 2): (a) Pd edge of monometallic $Pd_{147}$ under $H_2$; (b) Pd edge of the $Pd_{147}@Cu_{162}$ intermediate under $H_2$; (c) Pd edge of the final $Pd_{147}Pt_{162}$ DENs under He; and (d) the corresponding Pt edge of the same structure.**

confirm the CVs and suggest at least some Pd is present on the surface of the $Pd_{147}Pt_{162}$ DENs. Importantly, the voltammetry of an electrode modified with $Pd_{147}Pt_{162}$ DENs is the same before and after the ORR (Figure S4), suggesting that the DEN structure is not altered by the electrocatalytic reduction of $O_2$. Additional credence for this claim is provided by TEM images obtained before and after the ORR (Figure S5), which show that the average particle size remains unchanged (2.0 ± 0.2 *vs* 2.1 ± 0.3, respectively).

***In Situ* XAS Structural Characterization.** Figure 6 shows R-space data for the Pd edge of the monometallic precursor $Pd_{147}$ and $Pd_{147}@Cu_{162}$ DENs, as well as the Pd and Pt edges of the $Pd_{147}Pt_{162}$ DENs. Analysis of the Pd EXAFS data for the monometallic $Pd_{147}$ DENs yields a Pd−Pd coordination number ($CN_{Pd-Pd}$) of 8.4 ± 0.6, which is in good agreement with the calculated value (9.0) for a perfect 147-atom cuboctahedron. Table S1 provides Pd−Pd bond length, $r_{Pd-Pd}$, value of 2.791 ± 0.003 Å, which is larger than for bulk Pd (2.7506 Å). This lattice expansion is probably due to formation of PdH, because the XAS spectrum was obtained *in situ* during $H_2$ purging and just prior to addition of $Cu^{2+}$.[32] After addition of $Cu^{2+}$, and subsequent reduction, results of the Pd K-edge EXAFS data analysis of the putative $Pd_{147}@Cu_{162}$ intermediate suggest that it maintains a stable core@shell structure. For example, the $CN_{Pd-Pd}$ is, within the uncertainty of the measurement, unchanged in the absence and presence of Cu (8.4 ± 0.6 *vs* 7.8 ± 0.7, respectively). If alloying or inversion had occurred, the calculated values from the model structures (Table 1) demonstrate that this value would be significantly lower due to reduced Pd−Pd interactions: 4.1 for an inverted particle and 4.6 ± 0.2 for a random alloy. The Pd edge data and fit for the $Pd_{147}@Cu_{162}$ DENs, thus, confirm the integrity of the Pd core during the Cu deposition step and also indicate some Pd−Cu interactions ($CN_{Pd-Cu}$ = 1.7 ± 0.9).

The Cu XANES spectra in Figure 7 follow the oxidation state of Cu throughout the *in situ* synthesis of $Pd_{147}Pt_{162}$ DENs. The first step in this process is reduction of the $CuSO_4$ salt by the hydrided Pd DENs. The most notable observation is that the spectrum for Cu present in the $Pd_{147}@Cu_{162}$ structure (Figure 7a, red) lacks the large white line component (compare to Figure 7b, black line), indicating that the Cu has been reduced. The XANES spectrum of Cu in the $Pd_{147}@Cu_{162}$ DENs is overlaid with that of a Cu reference foil in Figure 7a. For the $Pd_{147}@Cu_{162}$ DENs, there are oscillations in the EXAFS region indicative of nearest neighbor scattering. However, the oscillations are not as pronounced as in the case of bulk Cu, which has extended order not present in nanoparticles of this size. The final step of the synthesis of the $Pd_{147}Pt_{162}$ DENs is galvanic exchange Cu for Pt. This involves oxidation of the Cu shell back to $Cu^{2+}$. The Cu XANES spectrum obtained after this step (Figure 7b, red) overlays with the $CuSO_4$ standard (Figure 7b, black), indicating that the galvanic exchange reaction goes to completion.

The bottom part of Table 1 shows CNs extracted from EXAFS data for the $Pd_{147}Pt_{162}$ final product. These data were obtained from the simultaneous first-shell fitting of the Pd and Pt edges. The experimentally

**TABLE 1. CNs Obtained from the Fitting of Experimental $Pd_{147}@Cu_{162}$ and $Pd_{147}Pt_{162}$ DENs EXAFS Data Compared to Calculated CNs of Model Structures[a]**

| $Pd_{147}@Cu_{162}$ | | | | |
|---|---|---|---|---|
| | Experimental | Calculated | | |
| CN | $Pd_{147}@Cu_{162}$ | $Pd_{147}@Cu_{162}$ | $Pd_{147}Cu_{162}$ alloy | $Cu_{147}@Pd_{147}Cu_{15}$ |
| $CN_{Pd-Pd}$ | 7.8 ± 0.7 | 9.0 | 4.6 ± 0.2 | 4.1 |
| $CN_{Pd-Cu}$ | 1.7 ± 0.9 | 3.0 | 5.1 ± 0.2 | 3.3 |

| $Pd_{147}Pt_{162}$ | | | | |
|---|---|---|---|---|
| | Experimental | Calculated | | |
| CN | $Pd_{147}Pt_{162}$ | $Pd_{147}@Pt_{162}$ | $Pd_{147}Pt_{162}$ alloy | $Pt_{147}@Pd_{147}Pt_{15}$ |
| $CN_{Pd-Pd}$ | 4.8 ± 1.1 | 9.0 | 4.6 ± 0.2 | 4.1 |
| $CN_{Pd-Pt}$ | 2.6 ± 1.2 | 3.0 | 5.1 ± 0.2 | 3.3 |
| $CN_{Pt-Pt}$ | 10.9 ± 3.7 | 4.7 | 5.0 ± 0.2 | 8.7 |
| $CN_{Pt-Pd}$ | 1.3 ± 0.6 | 2.7 | 4.6 ± 0.2 | 3.0 |

[a] Alloy values are the average of 20 random alloy configurations.

determined CN values are compared to three theoretical structures: $Pd_{147}@Pt_{162}$, a $Pd_{147}Pt_{162}$ alloy, and an inverted $Pt_{147}@Pd_{147}Pt_{15}$ structure. The EXAFS data were found to most closely match the inverted $Pt_{147}@Pd_{147}Pt_{15}$ structure. Most strikingly, the $CN_{Pt-Pt}$ (10.9 ± 3.7) is much larger than would be expected for a complete Pt shell (calculated $CN_{Pt-Pt}$ = 4.7) or if the structure was alloyed (calculated $CN_{Pt-Pt}$ = 5.0 ± 0.2). Also, the total Pt-metal CN ($CN_{Pt-M}$) of 12.2 (the sum of $CN_{Pt-Pt}$ and $CN_{Pt-Pd}$) is larger than the total Pd-metal CN ($CN_{Pd-M}$) of 7.4 (the sum of $CN_{Pd-Pd}$ and $CN_{Pd-Pt}$). This implies that Pt is more fully coordinated than Pd, which would be expected if Pt is predominantly in the interior of the nanoparticle as surface atoms have fewer nearest neighbors.[33] A full summary of the extracted parameters from the EXAFS fits, including *r* and $\sigma^2$ values, can be found in Table S1 for all samples. A TEM micrograph of the $Pd_{147}Pt_{162}$ DENs prepared *in situ* is presented in Figure S6.

**DFT Calculations.** DFT calculations were used to better understand the observed inversion of $Pd_{147}Pt_{162}$ DENs. The thermodynamic stability of $Pd_{147}@Pt_{162}$ nanoparticles was evaluated using the segregation energy ($E_{seg}$), which is the energy required to swap a shell atom with its neighboring Pd-core atom. Negative values of $E_{seg}$ correspond to favorable exchange of atoms between the shell and core. The effect of an aqueous environment was taken into consideration by adsorbing a hydroxyl group (OH) to surface sites neighboring the swapped atom. Because Cu binds OH more strongly than Pd, the Cu shell is stabilized and the $Pd_{147}@Cu_{162}$ structure is predicted to be stable. This is the same result found in the aforementioned experiments.

Here we focus on the inversion of $Pd_{147}Pt_{162}$ DENs. The segregation energy for different sites on $Pd_{147}@Pt_{162}$ and Pd/Pt bulk are listed in Table 2. For $Pd_{147}@Pt_{162}$ in vacuum, the corner site has the most negative segregation energy (−0.26 eV), indicating that Pt atoms at corner sites are the least stable with respect to migration into the core. The presence of adsorbed OH groups does not significantly change the value of $E_{seg}$ for the (100) facet, or the edge and corner sites. However, $E_{seg}$ of atoms on the (111) facet, which is energetically unfavorable for swapping in the vacuum, drops to −0.27 eV in the presence of OH, becoming another reactive site for core−shell inversion.

Previous studies showed that Pt can form a stable monolayer on a bulk Pd surface and on large (~3.5−9 nm) Pd nanoparticles[3−6,10,34] Accordingly, the same thermodynamic stability calculations used for the DENs, with and without surface OH groups, were performed on 4-layer, 4 × 4 Pd(111) and Pd(100) slab models supporting a Pt monolayer. The calculated segregation energies of both bulk facets are almost the same (within 0.01 eV, Table 2) as for the DEN model. This calculation indicates the inversion we observed on

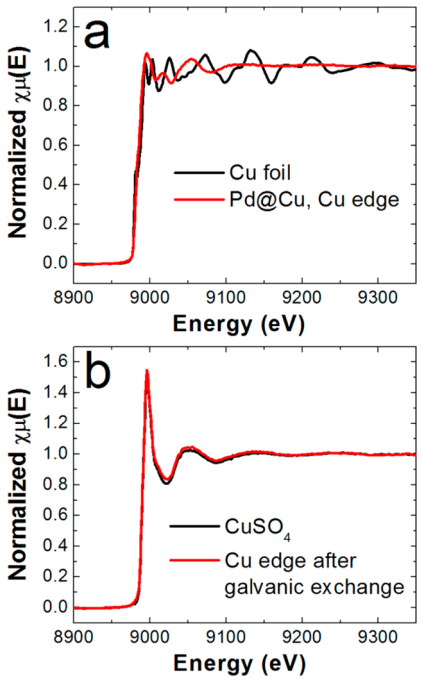


**Figure 7. Cu XANES of (a) a Cu foil and the reduced Cu shell of the $Pd_{147}@Cu_{162}$ structure and (b) a $CuSO_4$ solution (no dendrimer present) and the $Pd_{147}Pt_{162}$ DENs solution after the galvanic exchange step. The results indicate that the Cu shell is oxidized in the presence of $Pt^{2+}$.**

**TABLE 2. Summary of Segregation Energies of $Pd_{147}Pt_{162}$ Compared to Bulk Pd/Pt, with and without Surface Hydroxyl Present**

| | $Pd_{147}Pt_{162}$ | | | | Pd/Pt Bulk | |
|---|---|---|---|---|---|---|
| site | (111) | (100) | edge | corner | (111) | (100) |
| $E_{seg}$ (eV) | 0.04 | −0.17 | −0.06 | −0.26 | 0.03 | −0.18 |
| $E_{seg(OH)}$ (eV) | −0.27 | −0.11 | −0.05 | −0.27 | −0.28 | −0.11 |

$Pd_{147}Pt_{162}$ is likely due to the unstable corner sites. Within the context of this model, as the size of the nanoparticle increases, the ratio of corner sites to surface sites drops, and the inversion will be less likely to occur. In addition, a Pt monolayer on larger Pd particles is likely kinetically stabilized. The nanoparticles in this study are only 2 nm in diameter and, hence, have a relatively flexible structure as compared to bulk materials, which is expected to lower the barrier for atom swapping especially at low coordinated sites.

**$Pd_{55}Pt_{92}$ DENs.** To test for generality, we prepared $Pd_{55}Pt_{92}$ DENs using the same approach applied for the previously discussed $Pd_{147}Pt_{162}$ DENs. The starting material for this synthesis was G6-OH($Pd_{55}$) DENs, a shell of Cu was added, and then the Cu was exchanged for Pt. Characterization data can be found in the Supporting Information. UV−vis spectra (Figure S7) show the same trends as for the $Pd_{147}Pt_{162}$ DENs, and TEM images and sizing histograms indicate an average particle diameter of 1.7 ± 0.2 nm (Figure S8) for $Pd_{55}Pt_{92}$. EXAFS characterization was also performed on the final product of a homogeneous solution of $Pd_{55}Pt_{92}$ DENs at a concentration of 100.0 μM. The spectra were obtained under He gas to prevent oxidation, and R-space data and corresponding fits are presented in Figure S9. Extracted CNs (Table S2) indicate the inversion also occurs with this smaller size of DENs. As for the larger DENs, the most notable EXAFS result is the $CN_{Pt-Pt}$ of 8.1 ± 1.9, which is significantly higher than anticipated for a $Pd_{55}@Pt_{92}$ core@shell configuration (4.7). Table S3 contains a full summary of the extracted parameters from the EXAFS fits of the $Pd_{55}Pt_{92}$ DENs.

## SUMMARY AND CONCLUSIONS

In this paper, we have shown that bimetallic DENs can be prepared by a homogeneous route involving sequential formation of a Pd core, a Cu shell, and then galvanic exchange of the Cu shell for Pt. We anticipated that this approach would yield Pd@Pt core@shell DENs. However, all of the evidence presented in this paper suggests that the structure inverts into one that is Pt rich in the interior and Pd rich on the exterior. The EXAFS results, in particular, are quite clear on this point.

DFT calculations suggest that the high energy edge and corners sites present in these smaller nanoparticles may help initiate rearrangement to more stable structures. Additionally, the intrinsic disorder present in particles in this size range may contribute to this tendency to reorganize, while in bulk systems or in larger nanoparticles, the Pt monolayer may be kinetically stabilized. The mechanism of this rearrangement poses an interesting theoretical question and further investigation into this model system is a future direction of this research.

From the results in this study, and our earlier examination of PdAu DENs,[1] we conclude that inversion and structural instabilities, generally, are characteristic of nanoparticles having sizes of <~2−3 nm. These findings are important, because they suggest that in this size range slab models may not be appropriate for nanoparticles. This in turn points to the importance of directly comparing theory with exact (or nearly exact) experimental models for nanoparticles in this size range.

## METHODS

**Chemicals.** Sixth-generation, hydroxyl-terminated poly(amidoamine) (PAMAM) dendrimers (G6-OH) in methanol were purchased from Dendritech, Inc. (Midland, MI). The methanol was removed under vacuum and the dendrimers reconstituted in water at a concentration of 250.0 μM. The following chemicals were used as received: $K_2PtCl_4$ and $K_2PdCl_4$ were purchased from Acros Organics; $CuSO_4$ and NaOH from Fisher Scientific; and $NaBH_4$ from Sigma-Aldrich. For electrochemical experiments, high-purity $HClO_4$ was purchased from J.T. Baker and high-purity (99.999%) $O_2$ and Ar gases were purchased from Praxair. All solutions were made using deionized water

having a resistivity of 18.2 MΩ·cm (Milli-Q gradient system, Millipore).

**DEN Synthesis.** Pd DENs were synthesized as previously reported.[29] Briefly, a 2.0 $\mu$M solution of G6-OH PAMAM dendrimer was prepared from a 250.0 $\mu$M stock solution. To this, 147 equiv of $K_2PdCl_4$ were added from a freshly prepared 0.010 M stock solution, and this solution was stirred for 30 min. Next, a 10-fold excess of $NaBH_4$ was added from a 1.0 M stock solution, and the resulting solution was allowed to stir for 15 min. We refer to these materials as $Pd_{147}$ DENs, where 147 is the metal-ion: dendrimer ratio and also reflects the approximate number of Pd atoms in each DEN. The $Pd_{147}$ solution was then purged with $H_2$ for 30 min, and while still purging, excess unreacted $NaBH_4$ was removed by adding aliquots of a 10% $HClO_4$ solution until the pH of the solution reached ~3.0. Next, aliquots of 0.30 M NaOH were added to raise the pH to ~7.5, and then 162 equiv of $CuSO_4$ were added with continuous purging of the solution with $H_2$. After 15 min, the purge gas was changed to $N_2$ and the solution was purged for an additional 30 min. Finally, 162 equiv of $K_2PtCl_4$ were added from a freshly prepared 0.10 M stock solution. The resulting DENs were kept under $N_2$ until analysis to ensure their stability.

**Characterization.** UV−vis spectra were acquired using a Hewlett-Packard HP8453 spectrometer. Transmission electron microscopy (TEM) images were obtained using a JEOL-2010F TEM operating at 200 kV. Samples for TEM analysis were prepared by drying 3 $\mu$L of a $Pd_{147}Pt_{162}$ catalyst ink (a mixture of DENs and Vulcan carbon, described later) on a lacey carbon grid. TEM samples of DENs obtained after electrochemical analysis were prepared by wiping the electrode surface with the TEM grid so that a portion of the dried ink was transferred to the grid. The particles were sized using Gatan Digital Micrograph software. XPS analysis was carried out using a Kratos Axis Ultra spectrometer equipped with a monochromatic Al Kα radiation source. The XPS samples were dried on a glassy carbon (GC) chip, and peak positions were normalized to the C 1s peak position at a binding energy of 284.5 eV. STEM images and energy-dispersive X-ray spectroscopy (EDS) spectra were acquired on a JEOL JEM-ARM200F aberration-corrected microscope operated at 200 kV.

**Electrochemistry.** Cyclic voltammograms (CVs) were obtained in a 0.10 M $HClO_4$ electrolyte solution using a Au counter electrode and a $Hg/Hg_2SO_4$ reference electrode (CH Instruments, Austin, TX), which was calibrated daily against an eDAQ Hydroflex hydrogen reference electrode. All potentials were converted to, and reported relative to, the reversible hydrogen electrode (RHE) scale. For electrochemical measurements, a CHI 1202B potentiostat (CH Instruments) was used. Rotating disk voltammetry (RDV) employed a Pine Instruments AFASR rotator and E7R9 series GC disk working electrode having a geometric area of 0.248 $cm^2$.

For electrocatalytic measurements, the electrode surface was modified with a DEN-containing ink prepared by mixing 1.0 mg Vulcan carbon EC-72R per 1.0 mL of a solution containing 80% 2.0 $\mu$M DENs, 20% isopropyl alcohol, and 0.05% Nafion. After sonicating this mixture for several minutes, 10 $\mu$L of the ink was allowed to dry on the GC disk electrode. For CVs, the electrolyte solution was purged with high-purity Ar, and for RDV experiments the solution was purged with high-purity $O_2$.

**X-ray Absorption Spectroscopy (XAS).** XAS data were collected at beamline X18B at the National Synchrotron Light Source (NSLS) at Brookhaven National Laboratory. Reference foils were collected in transmission mode and the data fit to yield the amplitude factors ($S_0^2$) that contribute to theoretical EXAFS signals for each absorber (Pt or Pd). $S_0^2$ values of 0.89 for the Pd K edge and 0.87 for the Pt $L_3$ edge were used for analysis. $Pd_{147}$ DENs were prepared at a concentration of 50.0 $\mu$M and purged with 5% $H_2$ in He. After the analysis of the $Pd_{147}$@$Cu_{162}$ intermediate, the purging gas was changed to pure He to ensure stability of the DENs. For *in situ* experiments, the data were collected in fluorescence mode using a passivated implanted planar silicon (PIPS) detector. The data were analyzed using the IFFEFIT and Horae software packages.[35−37] For analysis of monometallic $Pd_{147}$ DENs and the $Pd_{147}$@$Cu_{162}$ intermediates under $H_2$, the Pd K edge was fit with FEFF6 theory[38] in R-space using a *k*-weight of 2 for the Fourier transforms. For the final structure, simultaneous first-shell fitting of both Pd and Pt edges was done using a *k*-weight of 2 and by constraining the bond lengths (*r*) and Debye−Waller factors ($\sigma^2$) for the Pd−Pt and Pt−Pd scattering paths to be equivalent as measured from either edge.[33]

**DFT.** DFT was used to calculate segregation energies of $Pd_{147}$@$Cu_{162}$ and $Pd_{147}$@$Pt_{162}$. All calculations were performed using the VASP code,[39,40] where electron correlation was evaluated within the generalized gradient approximation using the Perdew−Wang91 functional.[41] Core electrons were described with the projector augmented-wave method.[42,43] Kohn−Sham wave functions for the valence electrons were expanded in a plane wave basis set with an energy cutoff of 280 eV. The energy cutoff was increased to 400 eV, and the segregation energy of $Pd_{147}$@$Pt_{162}$ was found to vary by less than 0.01 eV. Spin polarization was tested and used as required.

The $Pd_{147}$@$Pt_{162}$ nanoparticles were modeled as 309 atom face-centered cubic (fcc) crystallites in the shape of a cuboctahedron with 147 core atoms and 162 shell atoms, which is consistent with the size of the synthesized DENs. A cubic box of side length 28 Å was used to contain the particle with a vacuum gap of at least 11 Å in all directions to avoid interactions between periodic images. A Γ-point sampling of the Brillouin zone was used for the isolated particles. All atoms in the nanoparticle were allowed to relax; geometries were considered optimized when the force on each atom was <0.01 eV/Å.

*Conflict of Interest:* The authors declare no competing financial interest.

*Acknowledgment.* We acknowledge support from the Chemical Sciences, Geosciences, and Biosciences Division, Office of Basic Energy Sciences, Office of Science, U.S. Department of Energy (Contract: DE-FG02-13ER16428 to R.M.C. and G.H. and DE-FG02-03ER15476 to A.I.F.). We thank D. Bahena for assistance with the STEM images and EDS acquisition. This instrument was supported by a grant from the National Institute on Minority Health and Health Disparities (G12MD007591). We thank the Surface Analysis Laboratory at the Texas Materials Institute and the National Science Foundation (Grant No. 0618242) for funding the Kratos Axis Ultra XPS used in this work. Use of the NSLS is supported by the U.S. Department of Energy, Office of Science, Office of Basic Energy Sciences, under Contract No. DE-AC02-98CH10886. Beamline X18B at the NSLS is supported in part by the Synchrotron Catalysis Consortium, U. S. Department of Energy Grant No. DE-FG02-05ER15688. R.M.C. thanks the Robert A. Welch Foundation (Grant F-0032) for sustained research support.

*Supporting Information Available:* TEM image of $Pd_{147}$ DENs, open circuit potential measurements obtained during the synthesis of $Pd_{147}Pt_{162}$ DENs, Pd XPS of partially oxidized $Pd_{147}Pt_{162}$ DENs, CVs of $Pd_{147}Pt_{162}$ before and after electrochemical experiments, TEM data for $Pd_{147}Pt_{162}$ DENs after electrochemical experiments, TEM data for $Pd_{147}Pt_{162}$ DENs synthesized *in situ* for EXAFS experiments, and UV−vis, TEM, and EXAFS R-space plots for the Pd and Pt edges of the smaller $Pd_{55}Pt_{92}$ DENs. Tabulated data for all extracted EXAFS parameters for both $Pd_{147}Pt_{162}$ and $Pd_{55}Pt_{91}$ DENs, as well as calculated CNs of model structures. This material is available free of charge *via* the Internet at http://pubs.acs.org.

## REFERENCES AND NOTES

1. Weir, M. G.; Knecht, M. R.; Frenkel, A. I.; Crooks, R. M. Structural Analysis of PdAu Dendrimer-Encapsulated Bimetallic Nanoparticles. *Langmuir* **2010**, *26*, 1137–1146.
2. Yancey, D. F.; Zhang, L.; Crooks, R. M.; Henkelman, G. Au@Pt Dendrimer Encapsulated Nanoparticles as Model Electrocatalysts for Comparison of Experiment and Theory. *Chem. Sci.* **2012**, *3*, 1033–1040.
3. Taufany, F.; Pan, C.-J.; Rick, J.; Chou, H.-L.; Tsai, M.-C.; Hwang, B.-J.; Liu, D.-G.; Lee, J.-F.; Tang, M.-T.; Lee, Y.-C.; *et al.* Kinetically Controlled Autocatalytic Chemical Process for Bulk Production of Bimetallic Core−Shell Structured Nanoparticles. *ACS Nano* **2011**, *5*, 9370–9381.

4. Wang, J. X.; Inada, H.; Wu, L.; Zhu, Y.; Choi, Y.; Liu, P.; Zhou, W.-P.; Adzic, R. R. Oxygen Reduction on Well-Defined Core−Shell Nanocatalysts: Particle Size, Facet, and Pt Shell Thickness Effects. *J. Am. Chem. Soc.* **2009**, *131*, 17298–17302.
5. Sanchez, S. I.; Small, M. W.; Zuo, J.-M.; Nuzzo, R. G. Structural Characterization of Pt−Pd and Pd−Pt Core−Shell Nanoclusters at Atomic Resolution. *J. Am. Chem. Soc.* **2009**, *131*, 8683–8689.
6. Zhang, J.; Mo, Y.; Vukmirovic, M. B.; Klie, R.; Sasaki, K.; Adzic, R. R. Platinum Monolayer Electrocatalysts for $O_2$ Reduction: Pt Monolayer on Pd(111) and on Carbon-Supported Pd Nanoparticles. *J. Phys. Chem. B* **2004**, *108*, 10955–10964.
7. Tessier, B. C.; Russell, A. E.; Theobald, B. R.; Thompsett, D. $Pt_{ML}$/Pd/C Core-Shell Electrocatalysts for the ORR in PEMFCs. *ECS Trans.* **2009**, *16*, 1–11.
8. Wang, Y.; Toshima, N. Preparation of Pd−Pt Bimetallic Colloids with Controllable Core/Shell Structures. *J. Phys. Chem. B* **1997**, *101*, 5301–5306.
9. Li, G.; Lu, W.; Luo, Y.; Xia, M.; Chai, C.; Wang, X. Synthesis and Characterization of Dendrimer-Encapsulated Bimetallic Core-Shell PdPt Nanoparticles. *Chin. J. Chem.* **2012**, *30*, 541–546.
10. Frenkel, A. I.; Wang, Q.; Sanchez, S. I.; Small, M. W.; Nuzzo, R. G. Short Range Order in Bimetallic Nanoalloys: An Extended X-ray Absorption Fine Structure Study. *J. Chem. Phys.* **2013**, *138*, 064202.
11. Wells, P. P.; Crabb, E. M.; King, C. R.; Wiltshire, R.; Billsborrow, B.; Thompsett, D.; Russell, A. E. Preparation, Structure, and Stability of Pt and Pd Monolayer Modified Pd and Pt Electrocatalysts. *Phys. Chem. Chem. Phys.* **2009**, *11*, 5773–5781.
12. Christoffersen, E.; Liu, P.; Ruban, A.; Skriver, H. L.; Nørskov, J. K. Anode Materials for Low-Temperature Fuel Cells: A Density Functional Theory Study. *J. Catal.* **2001**, *199*, 123–131.
13. Tan, T. L.; Wang, L.-L.; Johnson, D. D.; Bai, K. A Comprehensive Search for Stable Pt−Pd Nanoalloy Configurations and Their Use as Tunable Catalysts. *Nano Lett.* **2012**, *12*, 4875–4880.
14. Hansen, P. L.; Molenbroek, A. M.; Ruban, A. V. Alloy Formation and Surface Segregation in Zeolite-Supported Pt−Pd Bimetallic Catalysts. *J. Phys. Chem. B* **1997**, *101*, 1861–1868.
15. Duan, Z.; Wang, G. Monte Carlo Simulation of Surface Segregation Phenomena in Extended and Nanoparticle Surfaces of Pt−Pd Alloys. *J. Phys.: Condens. Matter* **2011**, *23*, 475301.
16. Huang, R.; Wen, Y.-H.; Zhu, Z.-Z.; Sun, S.-G. Pt−Pd Bimetallic Catalysts: Structural and Thermal Stabilities of Core−Shell and Alloyed Nanoparticles. *J. Phys. Chem. C* **2012**, *116*, 8664–8671.
17. Myers, V. S.; Weir, M. G.; Carino, E. V.; Yancey, D. F.; Pande, S.; Crooks, R. M. Dendrimer-Encapsulated Nanoparticles: New Synthetic and Characterization Methods and Catalytic Applications. *Chem. Sci.* **2011**, *2*, 1632–1646.
18. Bronstein, L. M.; Shifrina, Z. B. Dendrimers as Encapsulating, Stabilizing, or Directing Agents for Inorganic Nanoparticles. *Chem. Rev.* **2011**, *111*, 5301–5344.
19. Wilson, O. M.; Knecht, M. R.; Garcia-Martinez, J. C.; Crooks, R. M. Effect of Pd Nanoparticle Size on the Catalytic Hydrogenation of Allyl Alcohol. *J. Am. Chem. Soc.* **2006**, *128*, 4510–4511.
20. Ye, H.; Crooks, R. M. Electrocatalytic $O_2$ Reduction at Glassy Carbon Electrodes Modified with Dendrimer-Encapsulated Pt Nanoparticles. *J. Am. Chem. Soc.* **2005**, *127*, 4930–4934.
21. Myers, S. V.; Frenkel, A. I.; Crooks, R. M. X-ray Absorption Study of PdCu Bimetallic Alloy Nanoparticles Containing an Average of ∼64 Atoms. *Chem. Mater.* **2009**, *21*, 4824–4829.
22. Ye, H.; Crooks, R. M. Effect of Elemental Composition of PtPd Bimetallic Nanoparticles Containing an Average of 180 Atoms on the Kinetics of the Electrochemical Oxygen Reduction Reaction. *J. Am. Chem. Soc.* **2007**, *129*, 3627–3633.
23. Yancey, D. F.; Carino, E. V.; Crooks, R. M. Electrochemical Synthesis and Electrocatalytic Properties of Au@Pt Dendrimer-Encapsulated Nanoparticles. *J. Am. Chem. Soc.* **2010**, *132*, 10988–10989.
24. Carino, E. V.; Crooks, R. M. Characterization of Pt@Cu Core@Shell Dendrimer-Encapsulated Nanoparticles Synthesized by Cu Underpotential Deposition. *Langmuir* **2011**, *27*, 4227–4235.
25. Carino, E. V.; Kim, H. Y.; Henkelman, G.; Crooks, R. M. Site-Selective Cu Deposition on Pt Dendrimer-Encapsulated Nanoparticles: Correlation of Theory and Experiment. *J. Am. Chem. Soc.* **2012**, *134*, 4153–4162.
26. Iyyamperumal, R.; Zhang, L.; Henkelman, G.; Crooks, R. M. Efficient Electrocatalytic Oxidation of Formic Acid Using Au@Pt Dendrimer-Encapsulated Nanoparticles. *J. Am. Chem. Soc.* **2013**, *135*, 5521–5524.
27. Pande, S.; Weir, M. G.; Zaccheo, B. A.; Crooks, R. M. Synthesis, Characterization, and Electrocatalysis using Pt and Pd Dendrimer-Encapsulated Nanoparticles Prepared by Galvanic Exchange. *New J. Chem.* **2011**, *35*, 2054–2060.
28. Leff, D. V.; Ohara, P. C.; Heath, J. R.; Gelbart, W. M. Thermodynamic Control of Gold Nanocrystal Size: Experiment and Theory. *J. Phys. Chem.* **1995**, *99*, 7036–7041.
29. Carino, E. V.; Knecht, M. R.; Crooks, R. M. Quantitative Analysis of the Stability of Pd Dendrimer-Encapsulated Nanoparticles. *Langmuir* **2009**, *25*, 10279–10284.
30. NIST X-ray Photoelectron Spectroscopy Database, Version 4.1 (National Institute of Standards and Technology, Gaithersburg, 2012); http://srdata.nist.gov/xps/.
31. Knecht, M. R.; Weir, M. G.; Myers, V. S.; Pyrz, W. D.; Ye, H.; Petkov, V.; Buttrey, D. J.; Frenkel, A. I.; Crooks, R. M. Synthesis and Characterization of Pt Dendrimer-Encapsulated Nanoparticles: Effect of the Template on Nanoparticle Formation. *Chem. Mater.* **2008**, *20*, 5218–5228.
32. Rose, A.; Maniguet, S.; Mathew, R. J.; Slater, C.; Yao, J.; Russell, A. E. Hydride Phase Formation in Carbon Supported Palladium Nanoparticle Electrodes Investigated Using *in Situ* EXAFS and XRD. *Phys. Chem. Chem. Phys.* **2003**, *5*, 3220–3225.
33. Frenkel, A. I. Applications of Extended X-ray Absorption Fine-Structure Spectroscopy to Studies of Bimetallic Nanoparticle Catalysts. *Chem. Soc. Rev.* **2012**, *41*, 8163–8178.
34. Adzic, R. R.; Zhang, J.; Sasaki, K.; Vukmirovic, M. B.; Shao, M.; Wang, J. X.; Nilekar, A. U.; Mavrikakis, M.; Valerio, J. A.; Uribe, F. Platinum Monolayer Fuel Cell Electrocatalysts. *Top. Catal.* **2007**, *46*, 249–262.
35. Newville, M. IFEFFIT: Interactive XAFS Analysis and FEFF Fitting. *J. Synchrotron Radiat.* **2001**, *8*, 322–324.
36. Ravel, B.; Newville, M. ATHENA, ARTEMIS, HEPHAESTUS: Data Analysis for X-ray Absorption Spectroscopy Using IFEFFIT. *J. Synchrotron Radiat.* **2005**, *12*, 537–541.
37. Ravel, B. ATOMS: Crystallography for the X-ray Absorption Spectroscopist. *J. Synchrotron Radiat.* **2001**, *8*, 314–316.
38. Zabinsky, S. I.; Rehr, J. J.; Ankudinov, A.; Albers, R. C.; Eller, M. J. Multiple-Scattering Calculations of X-ray-Absorption Spectra. *Phys. Rev. B* **1995**, *52*, 2995–3009.
39. Kresse, G.; Hafner, J. First-Principles Study of the Adsorption of Atomic H on Ni (111), (100) and (110). *Surf. Sci.* **2000**, *459*, 287–302.
40. Kresse, G. Dissociation and Sticking of $H_2$ on the Ni(111), (100), and (110) Substrate. *Phys. Rev. B* **2000**, *62*, 8295–8305.
41. Perdew, J. P.; Wang, Y. Accurate and Simple Analytic Representation of the Electron-Gas Correlation Energy. *Phys. Rev. B* **1992**, *45*, 13244–13249.
42. Blöchl, P. E. Projector Augmented-Wave Method. *Phys. Rev. B* **1994**, *50*, 17953–17979.
43. Kresse, G.; Joubert, D. From Ultrasoft Pseudopotentials to the Projector Augmented-Wave Method. *Phys. Rev. B* **1999**, *59*, 1758–1775.